Astron. Astrophys. 323, 31–46 (1997)

ASTRONOMY AND ASTROPHYSICS

Interpretation of the emission line spectra of Seyfert 2 galaxies by multi-component photoionization models

Stefanie Komossa[1,2] **and Hartmut Schulz**[1,3]

[1] Astronomisches Institut der Ruhr-Universität, D-44780 Bochum, Germany
[2] Max-Planck-Institut für extraterrestrische Physik, D-85740 Garching, Germany
[3] Radioastronomisches Institut der Universität Bonn, Auf dem Hügel 71, D-53121 Bonn, Germany

Received 7 October 1996 / Accepted 9 December 1996

Abstract. We present multi-component photoionization models allowing for *local* density inhomogeneities in the NLR to interpret the emission line spectra of Seyfert 2 galaxies. This approach leads to a successful match of a large set of line intensities from the UV to the NIR. In particular, the hitherto elusive NIR features [SIII]λ9062 + λ9531 as well as high-ionization lines like [FeVII]λ6087 are consistently fitted. The predictions of CIII]λ1909 and CIVλ1549 are considerably improved.

From the detailed analysis of single-component photoionization models we derive the minimal radial extent of the NLR and the necessary span in density. Furthermore, we determine constraints on suggestions made about the role of matter-bounded clouds, and on proposed explanations for large [OIII]λ4363/λ5007 ratios (the so-called 'temperature problem'), and assess the usability of some emission-line ratios as indicators of the ionization parameter. We find that a *systematic* variation of the cloud column densities in a population of matter-bounded clouds is inconsistent with the trends and correlations exhibited by the emission lines in the diagnostic diagrams. Concerning the temperature problem, the only possibility that leads to an overall consistency with the strengths of all other observed emission lines is subsolar metal abundances (as compared to e.g. the presence of dust, the existence of a high-density component, or matter-bounded clouds).

In addition, the consequences of the presence of (Galactic-ISM-like) dust internal to the clouds were investigated. These models alleviate the [OIII]-ratio problem but did not lead to overall consistent fits. The most conspicuous fallacy lies in the extreme underprediction of Fe-lines, which is mainly due to the strong depletion of the Fe abundance.

In our final model series, the NLR is composed of a mixture of metal-depleted ($\sim$ 0.5 $\times$ solar) clouds with a radius-independent range in densities (10^2 to 10^5 cm^{-3}) distributed over a range of distances from the nucleus (galactocentric radii from at least $\sim 10^{20}$ cm to $10^{21.5}$ cm, for $Q_{\rm tot} = 10^{54}$ s^{-1}). In order to encompass the observed range of each line intensity relative to Hβ, it turns out to be necessary to vary the spectral energy distribution incident on the clouds, qualitatively confirming the findings of Ho et al. (1993). We found a successful continuum sequence by adding an increasing contribution of a hot black body ($T \approx 200\,000$ K) to a steep powerlaw ($\alpha_{\rm uv-x} \approx -2$). These continua imply that low and high-excitation objects differ in the strength but not in the basic shape of the EUV bump.

Key words: galaxies: active – galaxies: Seyfert – galaxies: nuclei – ultraviolet: galaxies

1. Introduction

The basic excitation mechanism for the emission lines of Seyfert galaxies is generally believed to be photoionization by radiation emerging from the central power source (e.g. Osterbrock 1989). If this is literally true in the sense that other heating and ionization mechanisms can be neglected for the formation of most of the emission-line spectrum, the well-established method of photoionization modeling can be employed to extract pertinent information about the central continuum source and the structure of the emission-line region. However, the history of AGN photoionizing modeling reveals some shortcomings despite a general success in fitting the gross features of the spectra.

Photoionization models exploring a *wide* range of parameters were first discussed by Stasińska (1984a,b). Although presenting mainly single-density models, she already emphasized the necessity of a multi-component approach. Ferland & Osterbrock (1986) and Binette et al. (1988) assumed the NLR to consist of a spherical system of individually optically thin filaments cumulatively becoming optically thick, with a radial dependence of density as $n(r) \propto r^{-1}$. In particular, Binette et al. noted that black bodies as ionizing continua are comparatively successful as powerlaws (PL).

Various density distributions of the narrow line gas (PL continuum-shape and the ionization parameter U kept constant)

Send offprint requests to: St. Komossa (Garching address), skomossa@rosat.mpe-garching.mpg.de

were studied by Viegas-Aldrovandi & Gruenwald (1988). Including relativistic electrons as an additional heating source they concluded that a combination of these processes with matter–bounded clouds provides the best fits to observed lines. Effects of intra-cloud density stratification were studied by Binette & Raga (1990). Recently, Ho et al. (1993) pointed out that correlations between certain line ratios could be attributed to the influence of a single parameter, the hardness of the ionizing continuum, parameterized in their models by the powerlaw index α.

Although in many respects successful, these models have a number of deficiencies in common. Whereas models involving powerlaw continua systematically underpredict the stronger observed HeIIλ4686 line intensities, pure black bodies (or geometrically thick accretion disks in the approximation of Madau 1988) fail to properly account for low ionization features like [SII]$\lambda\lambda$6716, 6731 (Binette et al. 1988, Acosta-Pulido et al. 1990). In addition, all pure photoionization models face the problems of (i) underpredicting the high ionization lines [NeV]λ3426 and CIII]λ1909, CIVλ1549 (by up to three orders of magnitude) whereas [OI]λ6300 is often reproduced too strong and (ii) leading to a too low electron temperature (indicated by the ratio [OIII]λ5007/[OIII] λ4363) as compared to observations. For those few predictions available for the recently measured [SIII]$\lambda\lambda$9069, 9532 lines in the near infrared (NIR) spectral region, no consistency with observations could be achieved in the sense that the predictions remain too strong (Osterbrock et al. 1992).

The aforementioned difficulties suggest that either the photoionization approach needs some modifications or that other ionizing or heating agents play a role as e.g. shocks. Detailed models including shock heating were presented by Viegas-Aldrovandi and Contini (e.g. 1989 and references therein). More recent models for fast shocks that include the photoionizing effect on the precursor gas of an ionizing continuum, which is produced in the shocked region, were discussed by Sutherland & Dopita (1995). Morphological evidence for shocked gas in Seyferts was recently summarized by Pogge (1996). However, whether these shocks also significantly contribute to the emission line excitation, is still unclear (cf. the critical review by Morse et al. 1996).

Here we test the classical assumption of pure photoionization equilibrium. Some of the pertinent results of the present study were earlier given in Komossa & Schulz (1994) and Komossa (1993, 1994). In the meantime photoionization studies were conducted by Moore & Cohen (1994,1996) and by Binette et al. (1996) who both invoke, albeit in different ways, a significant contribution of matter-bounded clouds to the emission line spectrum. They concentrate either on a few selected emission lines plus the additional information from line profiles or on a small sample of objects.

Our approach is to take a large sample of objects, to use all available emission lines, and to relax some classical but possibly doubtful assumptions on the interstellar-medium-(ISM)-like NLR gas that produces the narrow-line emission. For instance, rather than assuming a special radial density law to ensure cloud confinement by a supposed wind, we allow for an inhomogeneous ISM with a *range of densities* at the same galactocentric radius. *A priori*, other parameters are unconstrained as well. We have been reinforced to this approach by the success to find composite models for the extended narrow line region (ENLR) of NGC 4151 (Schulz & Komossa 1993).

The additional freedom leads necessarily to an 'explosion' of the parameter space. In order to narrow down the range of possibilities we therefore reinvestigate the response of the line spectrum to the radial extent of the NLR, the gas densities, the metal abundances, the spectral energy distribution and the cloud column densities. We also study the consequences of the inclusion of dust. The results are finally used to construct a multi-component model with the goal to resolve the aforementioned difficulties and find the essential parameter(s) that explain(s) *the ranges and correlations* exhibited by the Seyfert 2 data in the various diagnostic diagrams rather than fitting any individual object that might require some fine-tuning with regard to its own peculiar properties.

2. Conventions and abbreviations

Throughout this paper arguments of the log function are the physical quantities in cgs units. The powerlaw index α is defined in the sense that the flux distribution $f_\nu \propto \nu^\alpha$.

If not stated otherwise, all line intensities are simply denoted by the spectroscopic designation of the features in question (in unambiguous cases also the wavelength is omitted), and the numerical values are given as intensity ratios relative to Hβ.

3. Data base

In general, for investigating an object class there are two different types of approaches: either one can study one or a few well-observed individual objects, with the advantage of a more detailed and accurate treatment but at the risk of misidentifying the truly representative characteristics, or study a large sample of objects that is usually based on a more inhomogeneous data base but allows to utilize the information contained in collective trends and correlations so that true class properties might be revealed.

Here we follow the second approach in order to study group properties of Seyfert 2 galaxies. The necessary measured emission-line ratios from the UV to the NIR were compiled from Ferland & Osterbrock (1986), Koski (1978), Shuder & Osterbrock (1981), Phillips et al. (1983), Veilleux & Osterbrock (1987) and Osterbrock et al. (1992). A few objects were omitted that had later turned out to have to be differently classified. The objects chosen for the present study are listed in the caption of Fig. 1. For a homogeneous correction for dust reddening we utilized the average galactic extinction curve as listed in Table 7.2 of Osterbrock (1989) and an intrinsic value of Hα/Hβ = 3.1. For the remaining 18 out of 37 objects less complete data were taken from Veilleux & Osterbrock (1987) and (for the near-infrared [SIII] and [OII] lines) from Osterbrock et al. (1992). For easy identification in the figures all objects are coded by

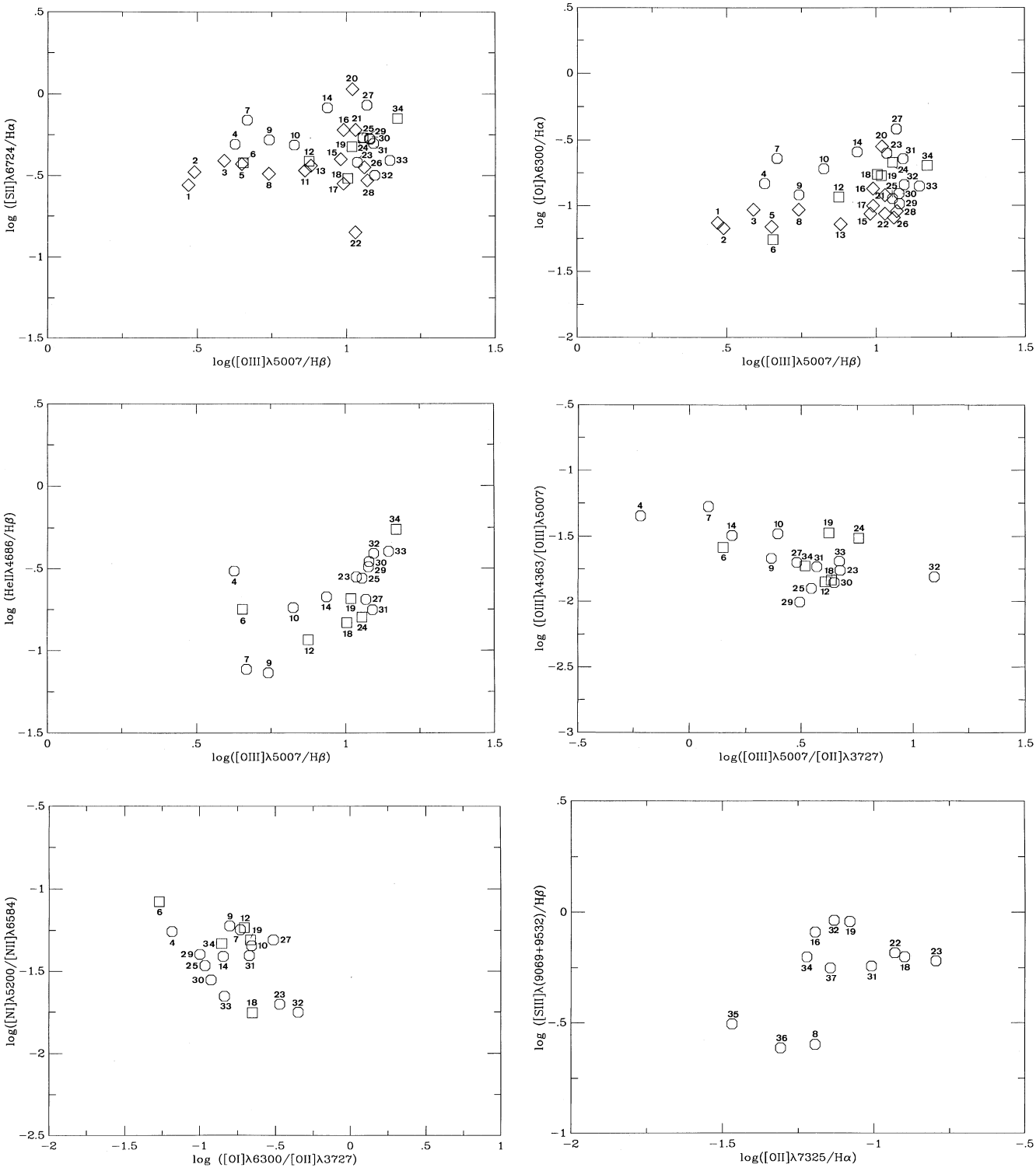

Fig. 1. Selection of log (line intensity ratio) diagnostic diagrams. Numbers correspond to object code as follows: 1 = Mrk 522, 2 = Mrk 599, 3 = Mrk 1066, 4 = Mrk 273, 5 = NGC 5256, 6 = Mrk 463W, 7 = Mrk 268, 8 = Mrk 917, 9 = Mrk 198, 10 = III Zw 55, 11 = MrkII 1125+581, 12 = Mrk 463E, 13 = Mrk 1073, 14 = Mrk 270, 15 = MrkII 1133+572, 16 = Mrk 1157, 17 = Mrk 1457, 18 = I Zw 92, 19 = NGC 4388, 20 = NGC 5655, 21 = Mrk 1058, 22 = Mrk 1388, 23 = Mrk 1, 24 = NGC 4151, 25 = Mrk 34, 26 = Mrk 403, 27 = Mrk 348, 28 = NGC 7674, 29 = Mrk 78, 30 = Mrk 573, 31 = Mrk 3, 32 = NGC 1068, 33 = Mrk 176, 34 = NGC 5643, 35 = IRAS 0147-074, 36 = IRAS 2021+112, 37 = NGC 5506. The objects in this sequence are ordered by strength in [OIII]/Hβ, with No. 1 corresponding to the lowest measured value for the sample, No. 37 to the highest.

the numbers given in Fig. 1. Plots of the most conspicuous line ratios are presented in Fig. 1. For comparison we included the Seyfert 1 galaxy NGC 4151 = No. 24.

The simplest AGN paradigm assumes that the ionization of the emission-line clouds is caused by the continuum radiation from a central 'point' source. Assuming in addition, that in the radio to IUE-UV and in the X-ray to gamma regions the central source is actually observed, a representative Seyfert continuum was constructed by pasting together piecewise powerlaws based on averages taken from the literature. We employed the following slope indices: in the IR: $\alpha_{100\mu-1\mu} = -1$, $\alpha_{1\mu-0.5\mu} = -2.1$ (Padovani & Rafanelli 1988); in the optical range: $\alpha_{\rm opt} = -1.5$ (Koski 1978); in the near to far UV: $\alpha_{\rm uv} = -1.4$ (Kinney et al. 1991); in the soft X-ray range: $\alpha_{\rm sx} = -0.5$ (Kruper et al. 1990); for harder X-rays: $\alpha_{\rm hx} = -0.6$ (Awaki et al. 1991, Mulchaey et al. 1992); and a break at 100 keV with $\alpha = -3.0$ beyond (cf. Fig. 2). These data fix the continuum outside the EUV range. However, the region between the Lyman limit and 0.5 keV ('EUV') is most important for the ionization. In general, this spectral region is not directly measurable due absorption by neutral gas between observer and object. For the models, in the EUV range the flux distribution was varied as described in Sects. 4.2.4 and 5.2, and we utilize the sensitivity of the line reaction on the EUV continuum to constrain the shape of the latter.

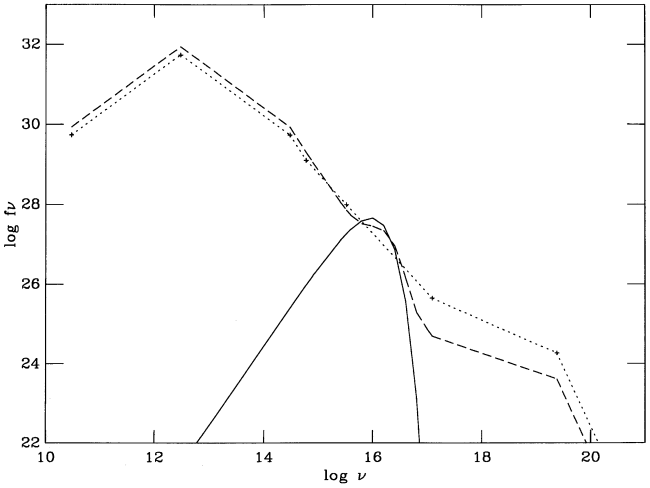

Fig. 2. Three selected spectral energy distributions used for the modeling. Continuous line: black body with $T_{\rm bb}$ = 160 000 K; dotted: powerlaw continuum with index $\alpha_{\rm uv-x} = -1.5$ in the EUV; dashed: sum of equal contributions of an EUV powerlaw with $\alpha_{\rm uv-x} = -2.0$ and a black body with $T_{\rm bb}$ = 200 000 K. Slopes for broken powerlaws outside the EUV region are taken from the literature (Sect. 3).

4. Inferences from single-component photoionization models

In order to set the stage for the multi-component models given in the next section, we first give a brief coherent account of the basic effects from the viewpoint of our one-component models. The calculations were carried out with version 84.03 of the photoionization code *Cloudy* (Ferland 1993). The program calculates the physical conditions in a plane-parallel slab of gas ionized and heated by the radiation field of a central object, by simultaneously solving the equations of statistical and thermal equilibrium. The resulting emission line spectrum is self-consistently predicted. For details, we refer to Ferland (1993). The calculation was stopped either when a pre-specified column density was reached (matter-bounded clouds) or when the equilibrium temperature dropped below 4000 K because emission of optical lines is then negligible (ionization-bounded clouds).

4.1. Parameter range

The photoionization models are characterized by:
(i) *The shape and strength of the ionizing EUV continuum.* We employ powerlaws with $\alpha_{\rm uv-x}$ from -1 to -2.5, black bodies with $T_{\rm bb}$ from 100 000 to 250 000 K and combinations of both (see Sect. 4.2.4). Examples of the continuum shapes considered are displayed in Fig. 2.

The luminosity of the continuum source is fixed by the total number rate $Q_{\rm tot} = 10^{54}$ s^{-1} of hydrogen ionizing photons isotropically emitted by the nucleus. Thereby the range of ionization parameters is essentially fixed meaning that other values of $Q_{\rm tot}$ are also encompassed after scaling the source–cloud distance range (see Sect. 4.2.1).
(ii) *The geometric and physical properties of the NLR.*

1. As representative distance(s) of the emission-line clouds from the central source we employed the four values $r_1 = 10^{20}$ cm, $r_2 = 10^{20.5}$ cm, $r_3 = 10^{21}$ cm, $r_4 = 10^{21.5}$ cm;
2. We considered as hydrogen column densities of the emission-line clouds $N_{\rm H} = 10^{18...24}$ cm^{-2}. For the adopted hydrogen densities, $N_{\rm H} = 10^{18}$ cm^{-2} always corresponds to matter-bounded clouds, 10^{24} cm^{-2} always to ionization-bounded clouds);
3. We systematically examined a range of total hydrogen densities $n_{\rm H} = 10^{2...6}$ cm^{-3} (a number of test calculations were also carried out with $n_{\rm H} = 10^0$ and 10^1 cm^{-3}).
4. Metal abundances were varied between 0.3 and 3 $\times$ the solar value (solar abundances are taken from Grevesse & Anders 1989).

The combination of (1) and (3) yields the ionization parameter U, defined as

$$U = Q_{\rm tot}/(4\pi r^2 cn) \quad (1)$$

where $n = n_{\rm H}$ is the total hydrogen number density. Given the range of values of $n_{\rm H}$ and r chosen, the models span a wide range of ionization parameters between $\log U = -6.58$ and +0.42.

4.2. Single-component models

Fig. 1 shows some of the diagnostically valuable line ratios. The data either form an uncorrelated cloud or correlations are apparent (the best examples being [OIII], [NeIII] and [FeVII] versus

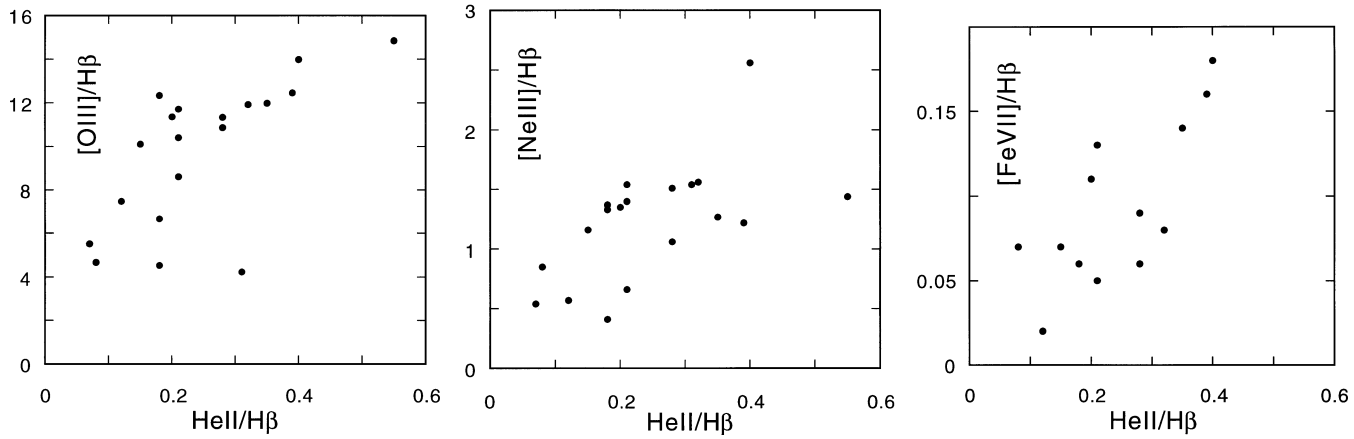

Fig. 3. Observed correlations for selected line-intensity ratios, [OIII]λ5007/Hβ, [NeIII]λ3869/Hβ, and [FeVII]λ6087/Hβ versus HeIIλ4686/Hβ.

HeII (Fig. 3)). After including 'high-excitation line' galaxies, Ho et al. (1993) found correlations in the [NII]–[OIII], [SII]–[OIII] and [OI]–[OIII] diagrams. In this section we explore the possibility whether such trends could be induced by the variation of a single model parameter (see also discussion in Ho et al. 1993) with special weight given to column-density effects. Generally, the effect of a single parameter variation depends on the choice of the other (fixed) parameters.

If not stated otherwise, *numerical* results given for illustration are for the models assuming solar elemental abundances and a 'reference continuum' with an EUV powerlaw of index $\alpha_{\rm uv-x} = -1.5$.

4.2.1. Distance of cloud from ionizing source

$Q_{\rm tot}$ and $r_1 \ldots r_4$ given above correspond to a range of H ionizing photon fluxes $\Phi = Q/(4\pi r^2)$ from 8×10^{12} phot cm^{-2} to 8×10^9 phot cm^{-2}. The distance range can be scaled to other values of Q because Φ is decisive as long as geometric effects are negligible.

Fig. 4 shows some of the basic results. As might be expected by the variation of U over the region, there is a clear trend that low-ionization lines (e.g. from [OII], [SII], [NI]) are formed at large radii while high-ionization lines (e.g. CIV, [NeIII], [NeV]) arise closer to the central source. A comparison with the observations leads to the more stringent conclusion that *all* line ratios cannot be simultaneously reproduced with clouds at only one distance. Moreover, the whole distance range assumed turns out to be necessary. E.g., the outermost distance r_4 is essential to model the low-ionization lines which would be too weak for any mixture of clouds at distances from r_1 to r_3 regardless of a wide range in density ($\log n_{\rm H} = 2 - 6$), metal abundance (solar or subsolar) and virtually all continua considered.

4.2.2. Hydrogen density

Using standard diagrams (e.g. Osterbrock 1989; his Fig. 5.3), the observed [SII]λ6716/λ6731 ratios yield electron densities of the order $n_{\rm e} \approx 10^{2-3}$ cm^{-3}, which could, however, be a misleading average over values from a much wider range of densities (cf. Mihalszki & Ferland 1983). Hence, we allow for hydrogen densities extending from $n_{\rm H} = 10^2$ to 10^6 cm^{-3}.

Fig. 4 also reveals the pronounced density dependence (but note that U is not constant). Most lines reach their maximal strength for $\log n_{\rm H} = 3 - 4$. Others, like [OI] (Fig. 4) and, depending on r, MgIIλ2798 and [SII]λ4072 increase towards higher densities and exceed all observed values at $\log n_{\rm H} = 6$.

On the other hand, CIVλ1549, [NeV]λ3426 and further high-ionization lines are strong at low densities. Even for constant U there is a notable density dependence. There is the expected trend (e.g. Filippenko & Halpern 1984, de Robertis & Osterbrock 1986) of higher emission close to the critical density (evident from Fig. 4 if points of the same value of U are connected; not drawn). However, if one also considers the radius dependence of the lines it is evident that the implied U variation over the NLR has a stronger effect than the closeness of the density to the critical density. This is, e.g., demonstrated in Fig. 4 by the behavior of [OIII]λ5007 and [NeV]λ3426.

The comparison with the observations reveals that it is neither possible to fit all observed lines with a single density nor could the observed trends be explained by a density variation. An appropriate mixture of components with different densities is required. The amount of the contribution of a possible high-density component ($\log n_{\rm H} = 5 - 6$) is limited by the extreme strength of some features like [OI] at these densities.

4.2.3. Metal abundances

We investigated metal abundances between 0.3 and 3 relative to the solar value. The value of the metal abundance influences the density of emitting metal ions and the equilibrium temperature. The temperature is important for the efficiency of the collisional excitation. Therefore, changing the abundance of a strong coolant affects many lines. Often the individual variation of the S and N abundances has no effect on lines from other species. In this case one can improve the fit of lines from S and N ions by tuning the corresponding abundances. In general, the

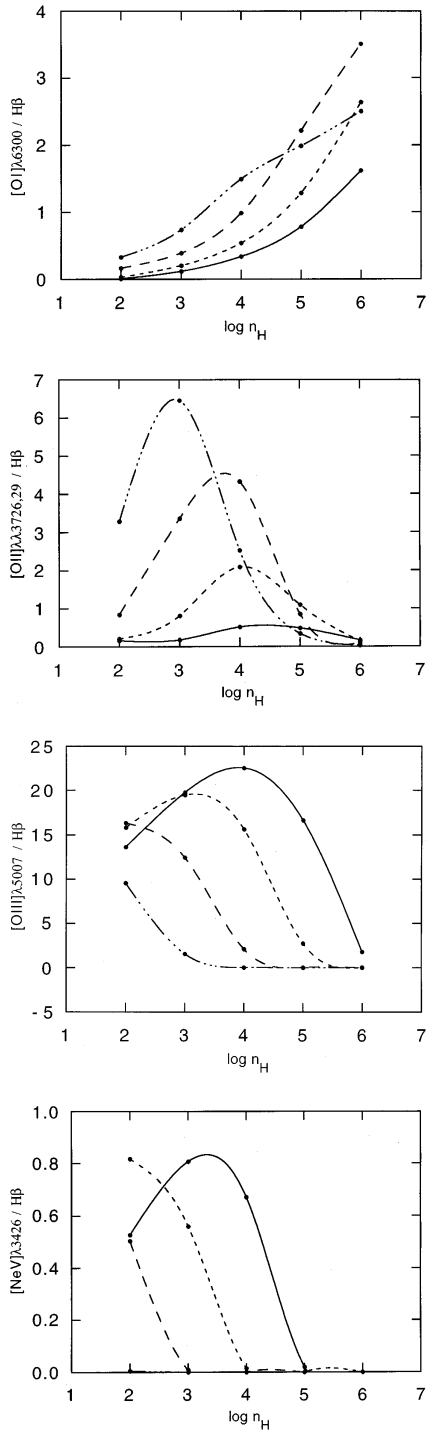

Fig. 4. Selected emission-line ratios versus hydrogen density. The lines connect points for constant radial distance r_i to the central source (continuous: $r_1 = 10^{20}$cm; short-dashed: $r_2 = 10^{20.5}$cm; long-dashed: $r_3 = 10^{21}$cm; dash-dotted: $r_4 = 10^{21.5}$cm; cf. Sect. 4.1). The critical densities for the individual lines are (in cm^{-3}) $n_{\rm crit}^{\rm [OI]} = 1.8\,10^6$, $n_{\rm crit}^{\rm [OII]} = 4.5\,10^3$, $n_{\rm crit}^{\rm [OIII]} = 7.0\,10^5$, and $n_{\rm crit}^{\rm [NeV]} = 1.6\,10^7$.

reduction of metal abundances leads to a lower sensitivity of the emission-line spectra on the continuum shape.

With suitable parameter choices, most line ratios can be predicted to yield acceptable fits for solar metal abundances or even above solar. The clear exception is [OIII]$\lambda5007/\lambda4363$ which is temperature sensitive below $n_{\rm e} \approx 10^5$ cm^{-3} and therefore signifies that strong coolants should be suppressed or other heating mechanisms be introduced.

4.2.4. Spectral energy distribution

For the observable part of the representative continua piecewise powerlaws were adopted as outlined in Sect. 3. In the important EUV part we employed a series of pure powerlaw continua with $\alpha_{\rm ux} = -2.5$ to -1 and continua with an additional contribution (20% to 100% of the total rate of ionizing photons $Q_{\rm tot}$) of hot black bodies with temperatures in the range 100 000–250 000 K. A few selected continua are shown in Fig. 2.

Since the adopted mean continuum has been composed using average slopes we made test calculations in order to check the influence of a possible scatter in the observed part (outside the EUV) of the flux distributions of individual galaxies. Varying (even to cutting-off) the continuum at wavelengths longer than the Lyman limit has a negligible effect, as expected. Cutting off the total radiation with photon energies exceeding 0.5 keV leads to a small but insignificant change of the line ratios. Only a strong increase of the X and γ–contribution boosts low-ionization and weakens high-ionization lines, especially for small radii, small densities and low metal abundances.

In contrast to the observed IR-UV and X-γ sections of the continuum, the shape of the EUV part has a strong influence on the emission-line spectrum, which, in turn, may be used for its determination.

Generally, an increase of the slope index α from -2.5 to -1 in powerlaw EUV continua strengthens most line intensities relative to Hβ. For solar abundances the strongest [NII] lines in our sample require $\alpha_{\rm uv-x} = -1$. Despite its hardness, such a flat powerlaw cannot generate most of the strongest observed [NeV] and HeII lines. Also, the 'canonical' powerlaw with $\alpha_{\rm uv-x} = -1.5$ is not able to reproduce the total set of line ratios in the observed ranges.

With black-body EUV continua, increasing $T_{\rm bb}$ has a similar effect as flattening an EUV powerlaw. All line ratios relative to Hβ considered here are strengthened except those of HeI. The strongest HeII, [NeV] and [FeVII] lines can be reached. However, the most intense CIII] lines can only be reproduced with $T_{\rm bb} = 250\,000$ K (at r_2 and for $\log n_{\rm H} = 4$).

If the observed range in HeII is due to a corresponding range of black-body temperatures then all observed lines should be correlated with HeII. Some strong lines like [NeIII] and [OIII] indeed confirm this expectation, whereas [NI] shows, if any, a slight anticorrelation with HeII in our Seyfert 2 sample. For a larger sample including more types of emission-line galaxies, Viegas-Aldrovandi (1988) found an anticorrelation in both [NI] and [OI] with HeII and suggested as an explanation a system-

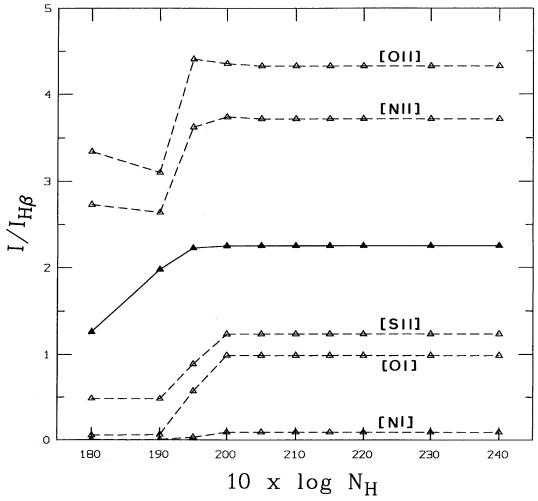

Fig. 5. Line intensity variations (relative to Hβ) in dependence of column density $N_{\rm H}$ of the emission-line cloud. The lines are selected for their *similar* behavior. From top to bottom (dashed): [OII]λ3727, [NII]λ6583, [SII]λ6731, [OI]λ6300, [NI]λ5200. For comparison, the variation of the total Hβ intensity (solid line, in arbitrary units) is plotted.

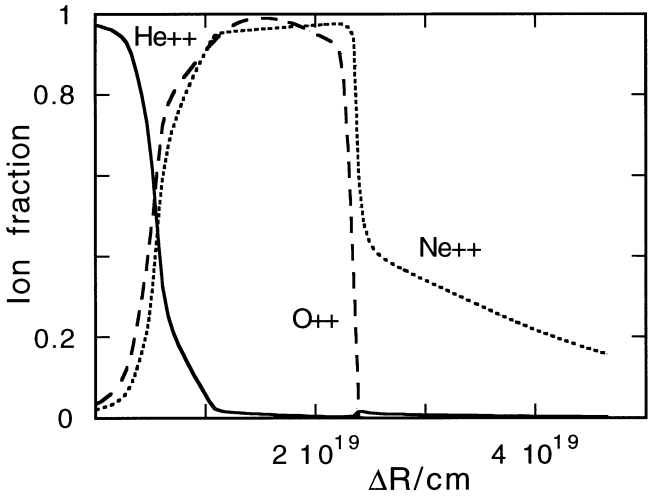

Fig. 6. Stratification of selected ions in an emission-line cloud, ion fraction versus cloud thickness ΔR, which explains the opposite behavior of [NeIII] and the recombination line HeII in most models.

atically increasing contribution of matter-bounded clouds. We shall pursue this idea in the next section.

Summarizing the results we conclude that it is not possible to explain the total range of Seyfert 2 line ratios with a single fixed EUV continuum shape.

4.2.5. Column density

Given the fragmentary structure of the interstellar medium, the existence of matter-bounded material in the NLR does not appear unlikely. The knowledge of the presence of such a component is important, e.g., for the determination of the anisotropy of the ionizing continuum (via the ionization-parameter sensitive [OII]/[OIII] ratio) or for estimating temperatures of the emitting gas (via the [OIII]λ4363/λ5007 ratio).

Hydrogen column densities in the range $N_{\rm H} = 10^{18}$ to 10^{24} cm^{-2} were considered to address the question whether the line-ratio correlations can be explained by a population of matter-bounded clouds. We found the following difficulties with this scheme:

First, the stronger and, hence, more accurately measured [NII], [SII] and [OI] lines are predicted to vary with column density in essentially the same way as [NI]. However, in our sample [NII], [SII] and [OI] are not anticorrelated with HeII as is claimed for [NI] (cf. Sect. 4.2.4).

Second, there are severe difficulties to produce the [NI]–HeII anticorrelation by varying $N_{\rm H}$, although *a priori* such a relation is not unexpected because HeII increases with lowering $N_{\rm H}$ in contrast to [NI]. However, in order for [NI] to be at least at the lower limit of its observed strengths, large densities (around 10^4 cm^{-3}) are required while a sufficient response of HeII on the column density is only found for smaller densities. For the standard continuum (with $\alpha_{\rm uv-x} = -1.5$), not even an arbitrary mixture of clouds with different densities, column densities and radial distances could reproduce the observations. For flatter powerlaw continua ($\alpha_{\rm uv-x} \geq -1.5$) or hotter black bodies ($T_{\rm bb} \gtrsim 150\,000$ K), [NI] and HeII become stronger. Because it would be extremely contrived and inconsistent with other line-ratios, we did not further attempt to look for a mixture of matter-bounded models which matches the trend of this single diagram.

Third, any systematic variation of the column, which is sufficiently dominant to be seen as a trend in the weak [NI] line is expected to have a more profound effect on stronger lines with lower measurement errors. The best positive correlations in our data set are exhibited by the strong [OIII] and [NeIII] lines versus HeII (Fig. 3). Are these correlations in agreement with a systematic variation of $N_{\rm H}$? This must be denied because there is always an *anti*correlation of [NeIII] with HeII in the model predictions. This is also true for [OIII] in virtually all cases. This kind of behavior can be traced back to the stratification of the corresponding ions (Fig. 6).

In conclusion, the observed correlations between line ratios cannot consistently be reproduced by *systematically* varying the column density from object to object. Notwithstanding these cautionary remarks on systematic effects, a random contribution to the line emission by a population of matter-bounded clouds cannot be excluded and could have introduced some of the dispersion in the observations. However, we note that, given the typical ionization structure of a NLR cloud, a matter-bounded cloud is only expected to significantly contribute to a given emission line for a very small range in column density and strong fine-tuning will be required to explain individual objects within such an approach.

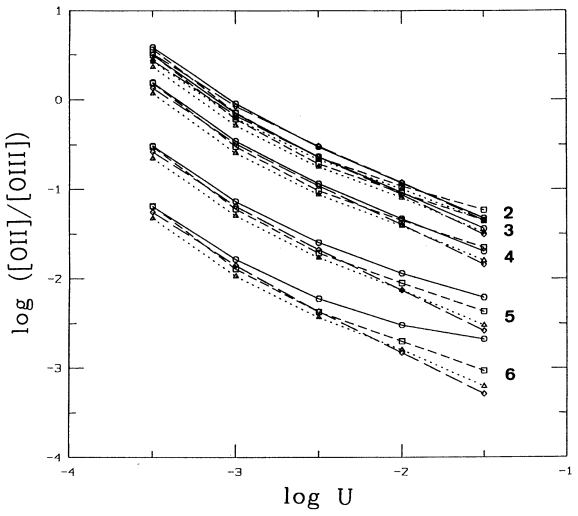

Fig. 7. Variation of [OII]/[OIII] with the ionization parameter U. Line ratios for constant continuum shape are connected by lines (continuous: powerlaw $\alpha_{\rm uv-x} = -1.5$; dashed: black body 230 000 K; dotted: black body 160 000 K; long-dashed: black body 100 000 K). The employed densities $\log n_{\rm H} = 2, 3, 4, 5, 6$ are marked at the right-hand side of the curves.

4.2.6. Indicators for the ionization parameter U

As a guide for modeling it would be helpful to have an indicator for U that is independent on other parameters. We briefly discuss the merits and deficiencies of two line ratios usable as U indicators.

[OII]λ3727/*[OIII]*λ5007. This line ratio has been previously used to estimate the value of U (e.g. Penston et al. 1990). As shown in Fig. 7, independent of continuum shape and for sufficiently low density ($n_{\rm H} < 10^3$ cm^{-3}) this line ratio yields U. However, for higher densities [OII]/[OIII] decreases with n due to the lower critical density of [OII] (4.5×10^3 cm^{-3}) as compared to [OIII] (7×10^5 cm^{-3}). If the actual NLR contains a mixture of densities the ratio predicts too high a value of U (Schulz & Komossa 1993). We also note that due to different excitation properties [OII] and [OIII] do not react in the same way on temperature changes induced by varying the metal or O abundance.

[NeIII]λ3869/*[NeV]*λ3426. This ratio is steeply dependent on U, but, in addition, it is also rather sensitive to the *shape* of the ionizing continuum because [NeV] requires ionizing photons exceeding 97.1 eV. The low sensitivity on density makes [NeIII]/[NeV] a good U indicator also for regions with density inhomogeneities provided the continuum shape is sufficiently well known.

5. Multi–component models

As discussed above, a single set of input parameters of one-cloud photoionization models is neither able to predict the observed strength of *all* observed emission lines nor does a variation of any single parameter yield a trend in agreement with the correlations observed. Consequently, we attempt to build a multi-component model that consists of clouds with different properties distributed over a certain radial extent.

5.1. Determination of the weights for radial distances and densities

Since the high-ionization and low-ionization lines are predominantly formed at small and large radii the full radius range considered here must be included (Sects. 4.1 and 4.2.1). The contribution of the innermost radius is limited by [NeV] to about 10% in Hβ. After detailed inspection of all models we finally fixed a 30% contribution in the Hβ luminosity by gas at each of the radii r_2, r_3 and r_4 and a 10% contribution of the gas at r_1.

For this mixture over radius we show the dependence of the most important line ratios as a function of density and continuum shape in Fig. 8. It is evident that, for a fixed continuum, the *range* of most observed lines can be covered by varying the density. However, it is not possible to obtain a consistent simultaneous solution of [OIII] and [OI].

Many lines are satisfactorily represented for $n_{\rm H} = 10^{3-5}$ cm^{-3}. However, a contribution of lower densities is necessary because the [SII] ratio indicates a lower average and lines from highly ionized species like CIV and [NeV] call for low-density gas at smaller radii.

A radially falling density law, e.g. $n \propto r^{-2}$ so that U = const, can be ruled out for the radius range considered in this paper e.g. by the strength of [NeV], which requires a higher than average U at the smaller radii.

From various density distribution functions studied, the one finally chosen equally weighs the lower hydrogen densities ($\log n_{\rm H} = 2, 3, 4$ with weight factors of 0.3) to correctly predict at the same time the high-ionization lines like [NeV] (which demands a high ionization parameter) as well as the low-ionization lines like [NII], [SII] (which originate further outwards preferentially at medium densities). The high-density end is limited by the strength of (then significantly boosted) [OI] leading to a weight of 0.1 for $\log n_{\rm H} = 5$.

5.2. Trends by varying the continuum shape

Having carried out an additional mixing over densities we are now looking for a parameter to sweep over the data clouds in the diagnostic diagrams. It turns out that by appropriate variation of the continuum shape the observed range of each line ratio is encompassed. The following results lead to constraints of the continuum: models with powerlaw continua cannot reach the strong HeII lines within the sample, which can, however, be matched with black body continua. Conversely, black bodies of the assumed temperature range lead to difficulties with the lower part of the [OIII] observations.

These findings suggest to combine a steep powerlaw with an increasingly dominating contribution of a hot black body. Below we adopt such an EUV continuum consisting of a powerlaw

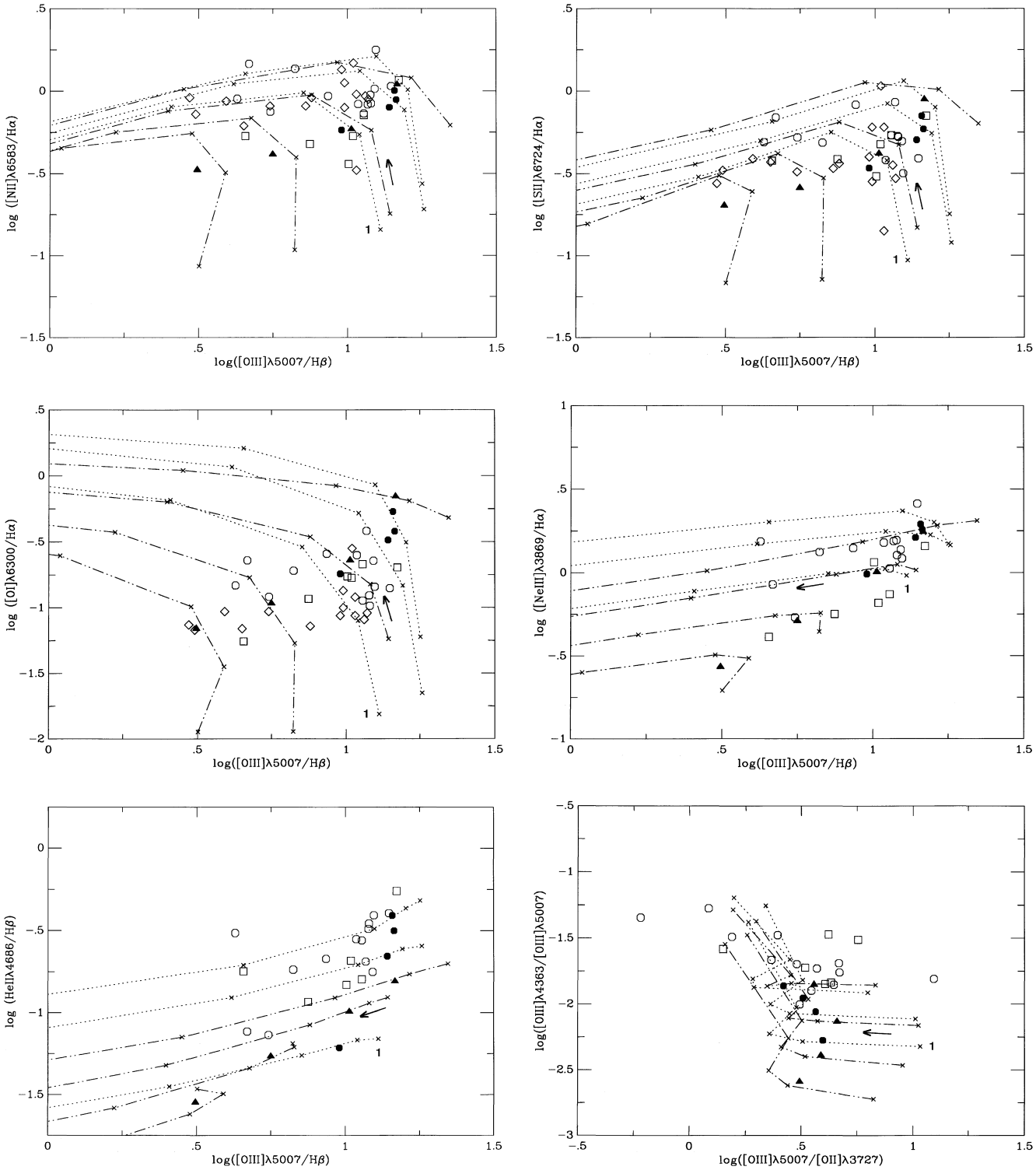

Fig. 8. These panels show selected diagnostic diagrams in which models and observations are compared. Open symbols denote observations. Model emission-line ratios represent a fixed mixture (see Sect. 5.1) over the four radii r_1 to r_4 and are connected by a line for each continuum shape. The dotted lines represent black-body continua with $T_{\rm bb}$ = 100 000 K (labeled '1' in the plots), 160 000 K and 250 000 K. The dot-dot-dashed lines refer to powerlaw continua with $\alpha_{\rm uv-x} = -2.5, -2.0, -1.5$ (the 'reference' continuum), and -1.0. The hydrogen density increases along each curve from 10^2 to 10^6 cm^{-3} (the direction is given by an arrow on the line of the reference continuum). Filled symbols denote model results for an additional mixture over density (Sect. 5.1). The triangles correspond to the powerlaw continua, the circles to the black body continua.

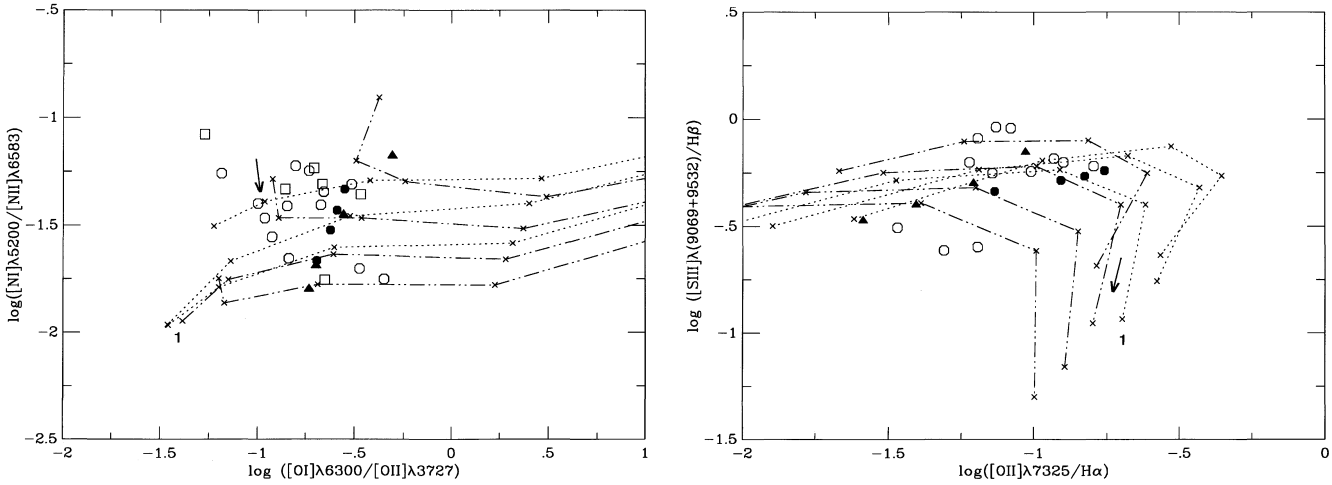

Fig. 8. Continuation.

with $\alpha_{\rm uv-x} = -2$ and a black body with $T_{\rm bb} = 200\,000$ K that contributes by 0, 20, 50, 80 and 100% to $Q_{\rm tot} = Q_{\rm pl} + Q_{\rm bb} =$ const.

5.3. The 'temperature problem'

Despite the general success of the approach in Sect. 5.2, for solar (or higher than solar) abundances one problem remains. Only the lower border of the observed temperature sensitive [OIII] ratios ($\lambda4363/\lambda5007$) is reached. In Fig. 9 we show various parameters that influence this ratio.

To boost it with a high-density ($> 10^5$ cm^{-3}) component could be possible for low radii (Fig. 9a), but would contradict the constraint set by [OI] which would then be significantly overpredicted.

As shown in Fig. 9b, matter-bounded clouds sufficiently strengthen the [OIII] ratio only for rather thin clouds with low surface brightness that are not very likely to dominate (see the discussion in Sect. 4.2.5) and, in addition, they lead to an overprediction of [OIII]/[OII].

Increasing the contribution of clouds at the lowest radius also leads to inconsistency with [OIII]/[OII] (Fig. 9a).

Photoelectric heating by dust leads to a higher electron temperature (Fig. 9c). However, dust causes further effects and will be discussed in more detail below (Sect. 5.4).

We are left with the reduction of the metal abundance to increase the [OIII] ratio (Fig. 9d). This also improves the predictions of [OI]. We finally fixed the metals to $0.5\times$ solar except sulfur ($0.75\times$ solar) and nitrogen (solar) because lines from N and S ions were weakened too much by the metal reduction.

5.4. Influence of dust

Covering the above ranges of all parameters except abundances and adopting the same precepts for mixing, models including dust mixed with the emission-line gas were computed. We adopted the Galactic-ISM typical dust composition of graphite and silicate incorporated in *Cloudy*, and including the correspondingly depleted ISM elemental abundances (Cowie & Songaila 1986).

We found some favorable properties of the inclusion of dust like an enhancement of [NeV] (by factors $\lesssim 3$) and HeII ($\lesssim 2$) (this is, however, not sufficient to obliviate the need of a black body component). CIV is weakened (by $\lesssim 3$) below the observed range while CIII] is strengthened in a way to better match the observations. (More detailed results are shown in Komossa 1993.)

The major deficiency of these models lies in the prediction of negligible intensities of all Fe lines due to the strong abundance depletion of Fe. This includes [FeIII]λ4658 and [FeVII]λ6087 which are believed to be formed in the 'regular' emission-line clouds. Lines from higher ionization species might be argued to essentially arise in a dust free extended component (e.g. Korista & Ferland 1989).

We conclude that models including dust of *Galactic ISM* properties and correspondently modified chemical abundances are not able to account for the observed Seyfert 2 spectra. Whether other dust compositions (e.g. mainly graphite to avoid the strong Fe depletion) could be successful is beyond the scope of the present paper; too many new free parameters are introduced in this case, to warrant a more detailed study at the present time.

5.5. Influence of cosmic radiation

The processes of heating and ionization by relativistic electrons in cosmic rays (protons in the usual energy range are much less efficient due to their large mass) are included in *Cloudy* (cf. Ferland & Mushotzky 1982). Adding these effects in the models by assuming the standard estimate for the Galactic density of cosmic ray electrons $n_{\rm cr} = 2\times10^{-9}$ cm^{-3} leads to negligible changes of the line ratios ($< 1\%$).

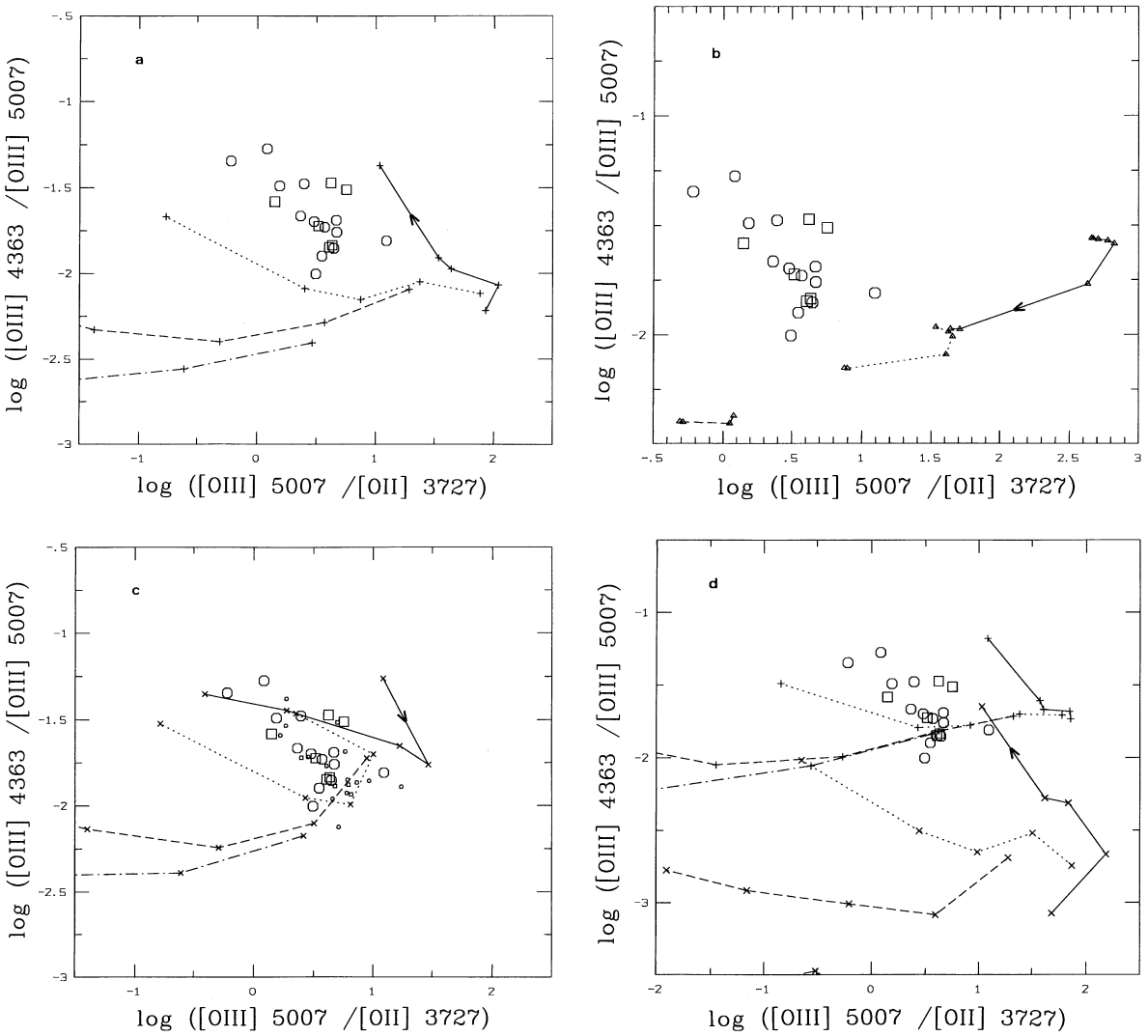

Fig. 9. a Dependence of the [OIII]λ4363/λ5007 ratio versus [OIII]λ5007/[OII]$\lambda\lambda$3726, 29 on cloud distance r_i and hydrogen density $n_{\rm H}$. Continuous, dotted, dashed and dot-dashed for $r_1 = 10^{20}$cm, $r_2 = 10^{20.5}$cm, $r_3 = 10^{21}$cm, $r_4 = 10^{21.5}$cm, respectively (Sect. 4.1). Along each line, $\log n_{\rm H}$ increases from 2 to 6 (direction indicated by the arrow). Solar abundances are adopted; **b** as in Fig. 9a, except that $\log n_{\rm H} = 4$ is kept constant and the column density is varied along the lines from $\log N_{\rm H} = 18$ to 24; **c** as in Fig. 9a, but now after including the effects of dust and correspondingly depleted elemental abundances. The small dots correspond to the original (not reddening corrected) observed line ratios; **d** as in Fig. 9a, except that the upper series of lines corresponds to metal abundances of 0.3 $\times$ solar and the lower series to 3.0 $\times$ solar.

5.6. The 'final' model series

The dust free metal–depleted series of multi-cloud models (Sect. 5.3), in which the EUV continuum varies by the percentage contribution of a 200 000 K black body added to a steep powerlaw, is taken as the basis for the discussion given below. This model sequence essentially accounts for the observed ranges of the emission-line intensities in the diagnostic diagrams (Fig. 10,11).

6. Discussion

After first discussing selected diagnostic diagrams we shall deal with the implications of the final model sequence.

6.1. The diagnostic diagrams

The main diagrams. Fig. 10 shows that the model sequence encompasses the observed ranges in the Veilleux-Osterbrock (1987) diagrams, i.e. [NII], [SII] and [OI] versus [OIII], and that it follows the main trends in HeII and [NeIII] versus [OIII].

Frequently, previous photoionization models encountered the difficulty of predicting too large [OI] intensities. For two objects, Viegas & Prieto (1992) solved this problem by truncating the column density of the clouds. Whereas this might be true for a few individual Seyferts (thereby explaining some of the observed scatter in [OI]) it seems improbable that in all objects the cloud-column densities adjust in such a way as to exactly match [OI].

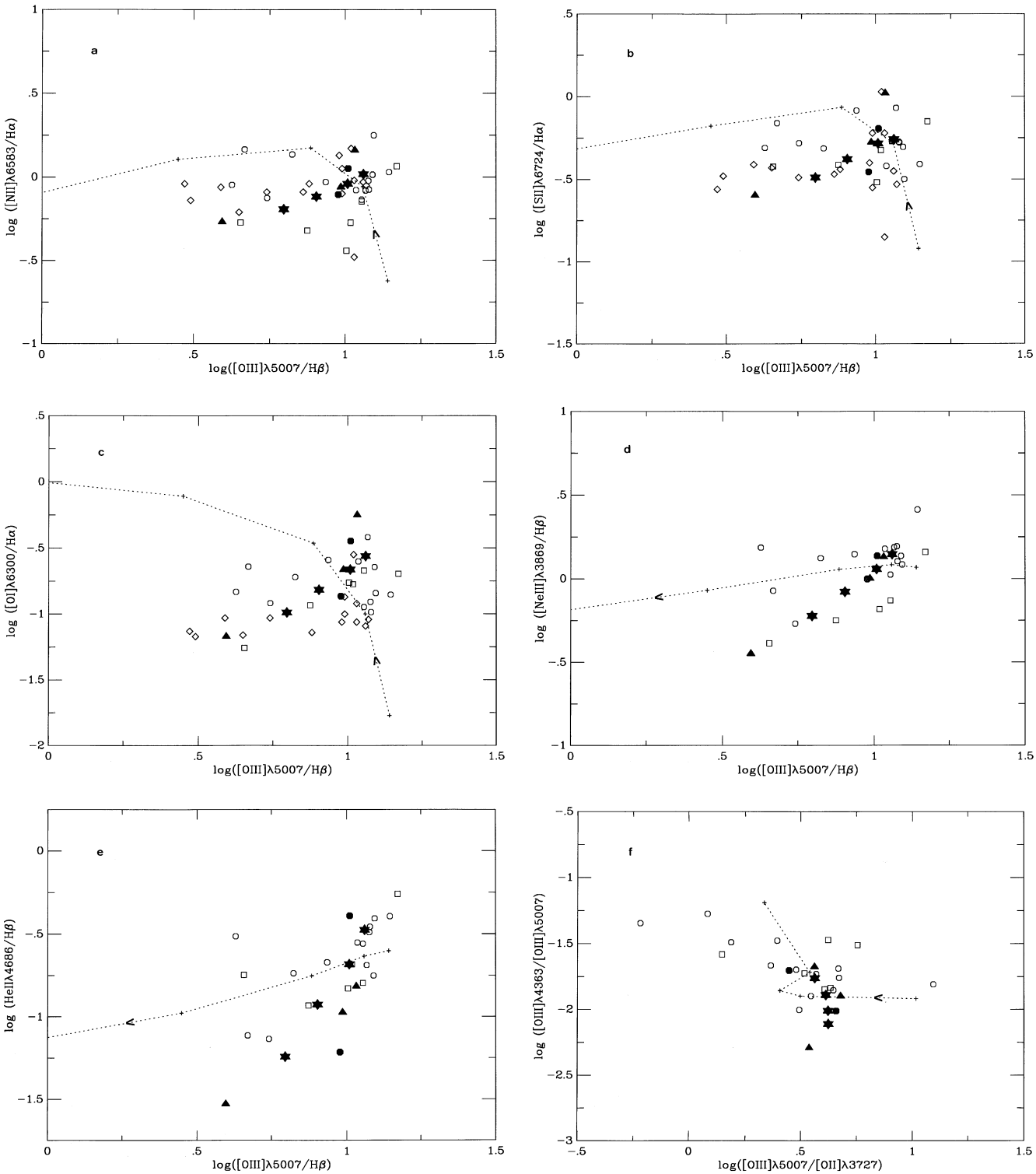

Fig. 10a–f. Comparison of the observations (open symbols) with multi-component models (fat symbols). The metals are reduced to 0.5 $\times$ solar. The models correspond to fixed mixtures over radius and density (Sect. 5.1). The four asterisk symbols in each diagram correspond to 0, 20, 50 and 100% contributions in Q of a 200 000 K black body (from bottom to top and left to right, respectively) added to an $\alpha_{\rm uv-x} = -2.0$ EUV powerlaw continuum. Fat triangles give the line ratios for powerlaw continua with $\alpha_{\rm uv-x} = -2.0, -1.5, -1.0$ (from bottom to top, respectively) and fat dots for black-body continua with $T_{\rm bb}$ = 100 000 and 250 000 K (bottom to top) for comparison. The dotted line shows the effect of the increase of the density from log $n_{\rm H}$ = 2..6 (direction indicated by arrow) for the fixed radius mixture and the standard continuum ($\alpha_{\rm uv-x} = -1.5$).

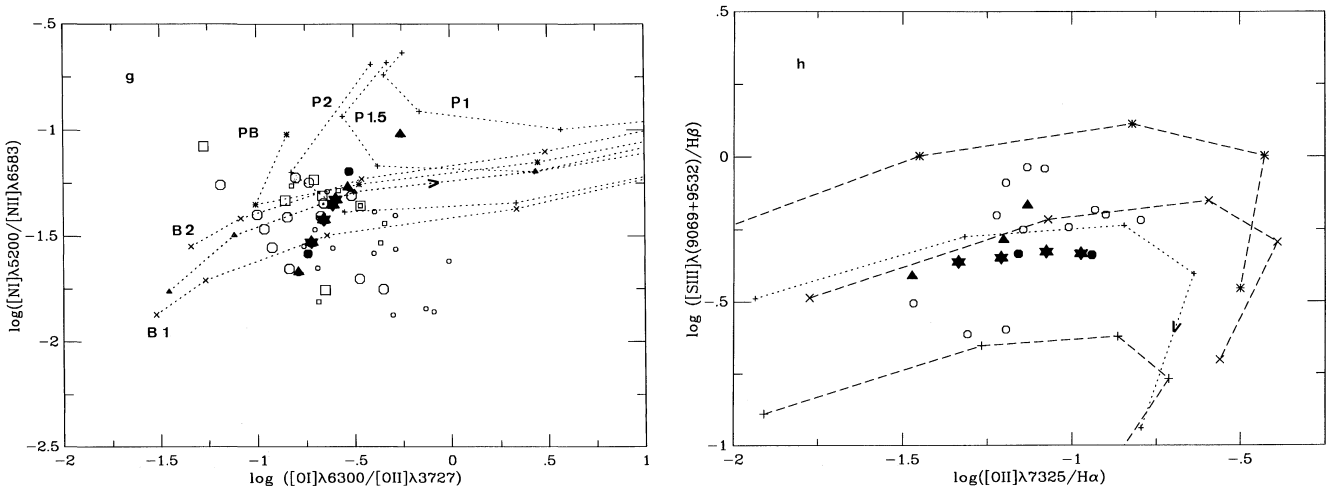

Fig. 10. g Continuation of Fig. 10. In this diagram we also show the original (not reddening corrected) data by small open symbols. The additional curves in this graph correspond to a range of models including dust as marked in the figure (Pa = powerlaw with index $\alpha_{\rm uv-x} = -a$, Bn = black body with $T = n \times 10^4$ K, PB = combination of P2 and B20 with a 50% contribution of each component). **h** NIR emission lines. In addition to the final model series, the effect of varying the chemical composition is shown (dashed lines), with metal abundances of (from top to bottom) (3.0, 1.0, 0.3) $\times$ solar.

Table 1. Emission line ratios $I/I_{\rm H\beta}$ for the final model sequence including those lines not shown in diagnostic diagrams, compared with the mean observed values <obs>. The abbreviations mark the form of the ionizing continuum: BB 20 = black body with $T = 20 \times 10^4$ K, PL 2 = powerlaw with index $\alpha_{\rm uv-x} = -2$, PB 50 = combination of PL 2 and BB 20 with a 50% contribution of each component. Note that not all objects contribute to each of the listed emission lines since some lines are only measured for a subsample; this particularly holds for CIV and CIII]. Also note that [NeV] and [ArIII] are at the borders of the range, in which optical spectra are taken. The listed observed values for all these lines are most probably biased towards high values.

line	<obs>	PL 2	PB 50	BB 20
CIV 1549	12.0	1.0	3.8	7.8
CIII] 1909	5.5	0.4	1.3	2.2
MgII 2798	1.8	1.5	2.9	3.1
[NeV] 3426	0.9	0.07	0.4	0.8
[OII] 3727	3.3	1.5	2.5	3.1
[NeIII] 3869	1.2	0.6	1.1	1.4
[SII] 4074	0.25	0.2	0.3	0.4
[OIII] 4363	0.2	0.05	0.1	0.2
HeII 4686	0.25	0.06	0.2	0.35
Hβ 4861	1.0	1.0	1.0	1.0
[OIII] 5007	9.1	6.2	10.2	11.5
[NI] 5200	0.1	0.1	0.1	0.1
HeI 5876	0.1	0.1	0.1	0.1
[FeVII] 6087	0.06	0.01	0.05	0.1
[OI] 6300	0.5	0.3	0.6	0.8
Hα	3.1	2.7	2.8	2.9
[NII] 6583	2.9	1.7	2.5	3.0
[SII] 6724	1.5	0.9	1.5	1.6
[ArIII] 7135	0.3	0.1	0.1	0.1
[OII] 7325	0.3	0.1	0.2	0.3
[SIII] 9069	0.5	0.3	0.4	0.4
[SIII] 9532	1.3	0.9	0.9	1.0

[OIII] ratio versus [OIII]/[OII]. Despite the 0.5 times reduction of the metal abundances the largest values of the [OIII]λ4363/5007 ratio cannot be reached. This would be possible with a metal depletion to 0.1 of the solar value, which, however, would call for a supposedly too strong tuning of the N and S abundances. However, the weak line [OIII]λ4363 is rather sensitive to measurement inaccuracies (note that five of the large [OIII] ratios plotted in Fig. 9 are denoted as uncertain by the observers). Furthermore, doubts on the reliability of older [OIII]λ4363 intensity measurements have recently arisen. Storchi-Bergmann et al. (1996) showed that the observed [OIII] tends to be *over*estimated due to improper subtraction of the galactic stellar spectrum.

The model sequence does not span the whole range in [OIII]/[OII]. This is a consequence of our assumption of a fixed cloud system exposed to a continuum sequence that only varies in shape, but with constant ionizing photon flux. In practice, some spread in the average ionization parameter $< U >$ is expected although the spectroscopic similarities between Seyferts and QSOs exclude gross variations in U over a wide luminosity range. Part of the scatter could be explained by a variation of the mean density (see below; Sect. 6.4).

[NI]/[NII] versus [OI]/[OII]. There is no model sequence that can explain the weakly apparent 'anticorrelation' in this diagram (Fig. 10h) and in particular the large [NI]/[NII] at low [OI]/[OII] values (called the '[NI] puzzle' by Stasińska (1984)). The diagram shows that the reddening correction has enhanced the problem. Although [NI]/[NII] is boosted in models including dust, compensating effects in [OI]/[OII] lead to avoidance of the upper left region (Fig. 10h). We note, however, that the two objects of our sample at the critical upper left of the diagram appear peculiar in several diagrams (see below).

In any case, it would be desirable to have more reliable measurements of the weak [NI]λ5200 line. The problem is on the low-ionization side where starburst components could be involved.

6.2. The NIR lines

[SIII]λ9069 + λ9532 *versus [OII]*λ7325. The near-infrared [SIII] lines are a useful aid for the classification of emission-line galaxies (Osterbrock et al. 1992; hereafter OTV). They might help to distinguish between different excitation mechanisms like photoionization or shock related processes (Diaz et al. 1985; Kirhakos & Phillips 1989). OTV noted that existing photoionization models of constant density predict these lines about a factor of three too strong. To remove this discrepancy, they suggested the possibility of density-mixtures, the presence of matter-bounded clouds or a lower abundance of sulfur.

However, calculations show that the effect by lowering the column density would be much too small. A strong decrease of the sulphur abundance would lead to a prediction of too weak *optical* [SII] lines. The multi-component models of the present work nicely reproduce the average of the observations. Whereas the observed span of the strong NIR [OII]λ7325 feature is well matched by the model sequence (Fig. 11b), the [SIII] observations show a larger scatter than the predictions of the final model sequence.

6.3. Further lines

CIII]λ1909 *and CIV*λ1549. These UV features have been measured for only six objects in our sample. Their large strength was difficult to be reached by previous models. Our predictions get closer to the observations, but still have problems in reproducing the highest observed values. Due to observational bias the few observed large line intensities might not be typical for AGNs. Upper limits that are considerably lower have recently been reported for seven radio-loud quasars by Wills et al. (1993) (upper limits of 0.56 to 2.2 for CIII]/Hβ and 0.64 to 2.4 for CIV/Hβ). Furthermore, it should be noted that the calculated lines are sensitive to uncertainties in the treatment of the Bowen resonance-fluorescence mechanism (cf. Ferland 1993).

Fe lines. [FeIII]λ4658 and [FeVII]λ6087 are consistently reproduced by our models while predicted lines from higher-ionization stages like [FeX]λ6374, [FeXI]λ7892 and [FeXIV]λ5303 are far below the observed values. However, as suggested by Korista & Ferland (1989) these lines might arise in a separate inter-cloud component of tenuous gas.

6.4. The scatter perpendicular to the mean model sequence

The scatter around the final model sequence often exceeds the measurement errors and therefore requires a separate explanation. In nearly all line-ratio diagrams a variation of the density $n_{\rm H}$ runs perpendicular to the final model sequence. Therefore, a variation of the density distribution could account for the scatter (Fig. 10).

This does, however, not work in the NIR [SIII]-[OII] diagram in which the model sequence is rather tight. Metal abundance variations may induce some of the scatter here (that usually lead to changes in the same direction as the continuum shape, although less pronounced, in most other diagrams).

We note that the original data (uncorrected for reddening) usually show the same trends in the line-ratio diagrams, i.e. our main results are rather insensitive to the exact value of reddening.

A few objects are conspicuous in the diagrams because they have a few exceptional line ratios that do not fit to the rest of the sample. E.g., Mrk 273 (No. 4 in Fig. 1) is exceptionally weak in [OIII] and exceptionally strong in [OII] and peculiar in further line ratios. NGC 1068 (No. 32) is exceptionally strong in [NII].

The presence of a contaminating starburst or HII component cannot be excluded in all cases, especially for the low ionization objects. So, also [NI] might be strengthened in a dusty starburst.

With these possibilities in mind it is not warranted to further tune our final model sequence which is remarkably successful, especially for normal to high ionization Seyfert 2s.

6.5. Implications of the multi-component model

The 'final' Seyfert 2 model consists of a radially distributed ensemble of clouds with densities $n_{\rm H}$ = 10^2 to 10^5 cm^{-3} and subsolar (except nitrogen) metal abundances exposed to the ionizing radiation of a continuum source in the center of the galaxy. The EUV continuum is characterized by a steep powerlaw plus a bump component, parameterized as hot black body the strength of which varies from object to object. Two questions arise: First, is this model in accordance with other observational evidence? Second, is there any model that would explain how the derived structure of the NLR could have formed and how it can be pertained? Having these questions in mind we in turn discuss the topics cloud origin, cloud confinement, and abundances.

Origin of the NLR gas, density range and cloud confinement. It is unclear how the NLR emission-line clouds are formed and how they are confined. Since the line widths suggest a relation to the dynamics of bulge stars (e.g. Wilson & Heckman 1985, Terlevich et al. 1990, Nelson & Whittle 1996) mass-loss of bulge stars might have delivered the material for the NLR clouds.

By noting that Seyfert nuclei host galaxies are early-type spirals, i.e. with large bulges, early speculations (e.g. Schulz 1986) suggested as a second possibility accretion of a dwarf galaxy.

In a third scenario proposed by Cameron et al. (1993) the NLR clouds arise from gas ablated from molecular-cloud complexes.

Concerning the density structure of the NLR, there might even be a density stratification within a single ionization-bounded entity identified as a 'cloud' but the lack of a detailed theory for such a structure hampers the application of appropriate photoionization models. Our approach of employing differ-

ent clouds each of constant density represents an approximation of the possibly more complicated real situation.

Photoionized clouds at the same radius but with different densities will attain quite different pressures so that a confinement problem may occur. For cloud thicknesses of the order of 10^{19} to 10^{21} cm sound crossing times are in the range $\sim 10^{5-7}$ years, which is on the orbital timescale in which destabilizing effects are likely to operate (cf. Mathews & Veilleux 1989). If clouds are destructed on short timescales one needs comparatively fast replenishment. The three mechanisms mentioned above could lead to a steady supply of NLR gas for more than 10^8 years so that requirements for cloud-confinement mechanism would be much relaxed.

Radial extent. The radial extend of the NLR gas refers to a model with fixed Q. Since the observed objects scatter in Q, our approach implies a scaling of NLR radius with object luminosity, similar to what is directly observed for the BLR (e.g. Peterson 1993).

Abundances. It is unclear which abundances are to be expected and a priori, there is no reason to expect them to be exactly solar. The question on the abundances is closely linked to the origin of the NLR gas. Our final model requires subsolar metal abundances of about 0.5 times the solar value.

Abundance determinations made with 'nebular methods' in HII regions within the spiral arms of a few Seyferts showed no strong differences to normal galaxies (Evans & Dopita 1987). On the other hand, Balcells & Peletier (1994) found subsolar metal abundances in spiral bulges. This would fit to the possible stellar origin of the NLR gas in Seyferts. Depleted gas-phase oxygen abundances were also found by Sternberg et al. (1994) in molecular gas in the central region of NGC 1068 and material evaporating from the torus may be an alternative reservoir for NLR clouds. In the same object, Marshall et al. (1993) found evidence for underabundant oxygen of 1/5 $\times$ solar in the warm electron scattering medium using X-ray data. Recently, in a large sample of spiral galaxies Zaritsky et al. (1994) derived a variety of O/H abundance ratios between 0.26 and 2.4 times the solar value.

Velocity field. In our final NLR model, high-ionization lines preferentially originate in clouds near the nucleus, whereas the major contribution to more lowly ionized species comes from further outwards. Consequently, a trend for a correlation of line-width with ionization potential is expected in case of decelerated outflow, accelerated inflow or rotation of the NLR material, whereas all lines are expected to have comparable line-widths in case of a dominating turbulent velocity component.

Whittle (1985) studied the line width variation versus ionization potential and critical density in a few Seyfert 2s and found only weak trends with no clear preference for either abscissa. This calls for a strong 'turbulent' (locally random velocity field) component, comparable to that found via a line-profile analysis e.g. in NGC 4151 (Schulz 1989, 1990).

EUV bump. One of the most remarkable features of the final model sequence is the varying dominance of the hot black body in the ionizing EUV. Although slightly narrower, this component might mimic the thermal component of an accretion disk. Another possibility would be that the black body crudely simulates a free-free component for $T < 10^6$ K.

In the IUE-UV of Seyfert 2s there is no indication for a rise towards shorter wavelength, so one might infer that the dominant temperature of a significant bump component must indeed be high. However, the absolute UV brightness of Seyfert 2s amounts only 10% of that of a typical Seyfert 1, so that rather than seeing the continuum source directly we are likely to see a scattered component in agreement with the unified model (e.g. Mulchaey et al. 1994). Adopting the 'unified view' that Seyfert 2s are more inclined Seyfert 1s it is justified to make a comparison with Seyfert 1 continua. Recent quasi-simultaneous UV – soft X-ray studies (Walter & Fink 1993; Walter et al. 1994) of Seyfert 1 galaxies indeed suggest the presence of an EUV component of varying strength but constant shape.

Independent evidence for the existence of EUV bumps comes from the so-called photon-deficit problem, one interpretation of which is the existence of an additional EUV bump component (e.g. Penston et al. 1990, Kinney et al. 1991).

7. Summary and conclusions

Emission-line spectra from 37 Seyfert 2 galaxies are utilized to find constraints for photoionization models that are required to fit all available lines. We discuss the influence of several parameters as are the radial extent of the NLR, the gas density, the cloud column density, the metal abundance, dust and the shape of the ionizing continuum. The results are used to build a multi-component NLR model, thereby solving or diminishing known problems in previous photoionization approaches, and to filtrate the parameter that governs the trends and correlations in the emission-line diagrams.

To explain both high and low ionization lines, emission-line gas has to be distributed over a range of galactocentric radii (of $\sim 10^{20}\sqrt{Q_{\rm tot}/10^{54}{\rm s}^{-1}}$ cm to $10^{21.5}\sqrt{Q_{\rm tot}/10^{54}{\rm s}^{-1}}$ cm). Furthermore, no single hydrogen density can account for all lines. The range covers $n_{\rm H} = 10^2$ to 10^5 cm^{-3}. Metal abundances must be subsolar ($\sim 0.5\times$ solar) for at least all objects with a measured [OIII]$\lambda4363/\lambda5007$ line ratio. This is found to be the only consistent solution to the 'temperature problem' for our sample, as compared to the possibility of the significant contribution of a high-density component ([OI] strongly overpredicted), the presence of dust internal to the NLR clouds (Fe lines underpredicted), or the contribution of matter-bounded clouds ([OIII]/[OII] overpredicted).

A *systematic* variation of the cloud column densities was found to be unsuccessful in explaining the trends and correlations in the diagnostic diagrams. Neither can it account for the clear correlation of e.g. [NeIII] with HeII, nor for the fact that [NI] is not clearly correlated with e.g. [OI] and [SII]. We cannot exclude a random contribution of matter-bounded clouds in individual objects, however.

We investigated powerlaw ($\alpha_{\rm uv-x} = -2.5$ to -1) and hot black-body components ($T_{\rm bb} = 100\,000$ to $250\,000$ K) in the EUV continuum. The highest values of HeII, [NeV] and CIII] can only be explained by including significant EUV bumps parameterized as black bodies. Irrespective of other parameters, a single fixed continuum shape cannot explain the total range of Seyfert 2 line ratios.

As a consequence of these results, we devised the following multi-component approach. The NLR is composed of an ensemble of ionization-bounded, metal-depleted clouds distributed over a range of radii, with a radius-independent mixture of densities. Along the model series in the emission-line diagrams (i.e. from one object to another), only the shape of the ionizing EUV continuum is varied. It consists of a steep powerlaw with $\alpha_{\rm uv-x} \approx -2$ plus a hot black body with a temperature $T_{\rm bb} \approx 200\,000$ K. The contribution of $Q_{\rm bb}$ to $Q_{\rm tot} = Q_{\rm pl} + Q_{\rm bb}$ spans 0 to 100%.

This model scheme matches the mean Seyfert 2 line ratios and reproduces the basic correlations. Deviations of individual objects from the mean can be introduced by, e.g., density variations.

Acknowledgements. We are indebted to Gary Ferland for providing *Cloudy*. H.S. acknowledges support by the German Space Agency DARA under 50 9102.

References

Acosta-Pulido J.A., Perez-Fournon I., Calvani M., Wilson A.S., 1990, ApJ 365, 119
Awaki H., Koyama K., Inoue H., Halpern J., 1991, PASJ 43, 195
Balcells M., Peletier R.F., 1994, AJ 107, 135
Binette L., Raga A.C., 1990, AJ 100, 1046
Binette L., Robinson A., Courvoisier T.J.-L., 1988, A&A 194,65
Binette L., Wilson A.S., Storchi-Bergmann T., 1996, A&A, in press
Cameron M., Storey J.W.V., Rotaciuc V., et al., 1993, ApJ 419, 136
Cowie L.L., Songaila A., 1986, ARA&A 24, 499
De Robertis M.M., Osterbrock D.E., 1986, ApJ 301, 727
Diaz A.I., Pagel B.E.J., Wilson I.R.G., 1985, MNRAS 121, 737
Evans I.N., Dopita M.A., 1987, ApJ 319, 662
Ferland G.J., 1993, University of Kentucky Department of Physics & Astronomy Internal Report
Ferland G.J., Mushotzky R.F., 1982, ApJ 262, 564
Ferland G.J., Osterbrock D.E. 1986, ApJ 300, 658
Filippenko A.V., Halpern J.P., 1984, ApJ 285, 458
Grevesse N., Anders E. 1989, in Cosmic Abundances of Matter, AIP Conf. Proc. 183, C.J. Waddington (ed.), New York: American Institute of Physics
Ho L.C., Shields J.C., Filippenko A.V., 1993, ApJ 410, 567
Kinney A.L., Antonucci R.R.J., Ward M.J., Wilson A.S., Whittle M., 1991, ApJ 377, 100
Kirhakos S., Phillips M.M., 1989, PASP 101, 949
Komossa S., 1993, Diplom thesis, Ruhr University, Bochum
Komossa S., 1994, in AGN across the electromagnetic spectrum, IAU-Symp. 159, T.J.-L. Courvoisier & A. Blecha (eds), 449
Komossa S., Schulz H., 1994, in The Analysis of Emission Lines (STScI Symp. contributed papers), R.E. Williams, M. Livio (eds), 30
Korista K.T., Ferland G.J. 1989, ApJ 343, 678
Koski A.T., 1978, ApJ 223, 56
Kruper J.S., Urry M.C., Canizares C.R., 1990, ApJS 74, 347
Madau P., 1988, ApJ 327, 116
Marshall F.E., Netzer H., Arnaud K.A., et al., 1993, ApJ 405, 168
Mathews W.G., Veilleux S., 1989, ApJ 336, 93
Mihalszki J.S., Ferland G.J., 1983, MNRAS 205, 1279
Moore D., Cohen R.D., 1994, ApJ 433, 602
Moore D., Cohen R.D., 1996, ApJ, in press
Morse J.A., Raymond J.C., Wilson A.F., 1996, PASP 108, 426
Mulchaey J.S., Mushotzky R.F., Weaver K.A., 1992, ApJ 390, L69
Mulchaey J.S., Koratkar A., Ward M.J., et al., 1994, ApJ 436, 586
Nelson C.H., Whittle M., 1996, ApJ 465, 96
Osterbrock D.E., 1989, Astrophysics of Gaseous Nebulae and Active Galactic Nuclei, (University Science Books: Mill Valley, CA)
Osterbrock D.E., Tran H.D., Veilleux S., 1992, ApJ 389, 196
Padovani P., Rafanelli P., 1988, A&A 205, 53
Penston M.V., Robinson A., Alloin D., et al., 1990, A&A 236, 53
Peterson B., 1993, PASP 685, 247
Phillips M.M., Charles P.A., Baldwin J.A., 1983, ApJ 266, 485
Pogge R., 1996, in Emission Lines in Active Galaxies: New Methods and Techniques, B.M. Peterson, F.-Z. Cheng, A.S. Wilson (eds), (San Francisco: Astronomical Society of the Pacific), in press
Schulz H., 1986, in Structure and Evolution of Active Galactic Nuclei, eds. G.Giuricin et al. (Reidel: Dordrecht), 705
Schulz H., 1989, in Extranuclear Activity in Galaxies, eds. E.J.A.Meurs & R.A.E.Fosbury (Garching: ESO; ESO Conf. No. 32), 417
Schulz H., 1990, AJ 90, 1442
Schulz H., Komossa S., 1993, A&A 278, 29 (Erratum (correction of printer's error): A&A 289, 662)
Shuder J.M., Osterbrock D.E., 1981, ApJ 250, 55
Stasińska G., 1984a, A&AS 55, 15
Stasińska G., 1984b, A&A 135, 341
Sternberg A., Genzel R., Tacconi L., 1994, ApJ 436, L131
Storchi-Bergmann T., Wilson A.S., Mulchaey J.S., Binette L., 1996, A&A, in press
Sutherland R.S., Dopita M.A., 1995, ApJ 439, 365
Terlevich E., Diaz A.I., Terlevich R., 1990, MNRAS 242, 271
Veilleux S., Osterbrock D.E., 1987, ApJS 63, 295
Viegas S.M., Prieto M.A., 1992, MNRAS 258, 483
Viegas-Aldrovandi S.M., 1988, ApJ 330, L9
Viegas-Aldrovandi S.M., Contini M., 1989, ApJ 339, 689
Viegas-Aldrovandi S.M., Gruenwald R.B., 1988, ApJ 324, 683
Walter R., Fink H.H., 1993, A&A 274, 105
Walter R., Orr A., Courvoisier T.J.-L., Fink H.H., Makino F., Otani C., Wamsteker W., 1994, A&A 285, 119
Whittle M., 1985, MNRAS 216, 817
Wills B.J., Netzer H., Brotherton M.S., et al., 1993, ApJ 410, 534
Wilson A.S., Heckman T.M., 1985, in Astrophysics of Active Galaxies and Quasi-Stellar Objects, ed. J.S.Miller (Mill Valley: Univ. Science), 39
Zaritzky D., Kennicutt R.C., Huchra J.P., 1994, ApJ 420, 87

This article was processed by the author using Springer-Verlag LaTeX A&A style file *L-AA* version 3.